J. Fluid Mech. (2008), *vol.* 601, *pp.* 339–364.
doi:10.1017/S0022112008000712 Printed in the United Kingdom

Supercritical transition to turbulence in an inertially driven von Kármán closed flow

FLORENT RAVELET†, ARNAUD CHIFFAUDEL AND FRANÇOIS DAVIAUD

Service de Physique de l'Etat Condensé, Direction des Sciences de la Matière, CEA-Saclay, CNRS URA 2464, 91191 Gif-sur-Yvette cedex, France

(Received 5 December 2006 and in revised form 18 January 2008)

We study the transition from laminar flow to fully developed turbulence for an inertially driven von Kármán flow between two counter-rotating large impellers fitted with curved blades over a wide range of Reynolds number ($10^2 - 10^6$). The transition is driven by the destabilization of the azimuthal shear layer, i.e. Kelvin–Helmholtz instability, which exhibits travelling/drifting waves, modulated travelling waves and chaos before the emergence of a turbulent spectrum. A local quantity – the energy of the velocity fluctuations at a given point – and a global quantity – the applied torque – are used to monitor the dynamics. The local quantity defines a critical Reynolds number Re_c for the onset of time-dependence in the flow, and an upper threshold/crossover Re_t for the saturation of the energy cascade. The dimensionless drag coefficient, i.e. the turbulent dissipation, reaches a plateau above this finite Re_t, as expected for 'Kolmogorov'-like turbulence for $Re \to \infty$. Our observations suggest that the transition to turbulence in this closed flow is globally supercritical: the energy of the velocity fluctuations can be considered as an order parameter characterizing the dynamics from the first laminar time-dependence to the fully developed turbulence. Spectral analysis in the temporal domain, moreover, reveals that almost all of the fluctuation energy is stored in time scales one or two orders of magnitude slower than the time scale based on impeller frequency.

1. Introduction

Hydrodynamic turbulence is a key feature of many common fluid mechanics problems (Tennekes & Lumley 1972; Lesieur 1990). In a few ideal cases, exact solutions of the Navier–Stokes equations are available, based on several assumptions such as auto-similarity, stationarity, or symmetry (for a collection of examples, see Schlichting 1979). Unfortunately, they are often irrelevant in practice, because they are unstable. Two of the simplest examples are the centrifugal instability of the Taylor–Couette flow between two concentric cylinders, and the Rayleigh–Bénard convection between two differentially heated plates: once the amount of angular momentum or heat becomes too great to be carried by molecular diffusion, a more efficient convective transport arises. Increasing further the control parameter in these two examples, secondary bifurcations occur, leading rapidly to temporal chaos, and/or to spatio-temporal chaos, then to turbulence.

† Present address: Laboratory for Aero and Hydrodynamics, Leeghwaterstraat 21, 2628 CA Delft, The Netherlands.

Several approaches have been taken in parallel concerning developed turbulence, focused on statistical properties of flow quantities at small scales (Frisch 1995) or taking into account the persistence of coherent structures in a more deterministic point of view (Tennekes & Lumley 1972; Lesieur 1990). One of the major difficulties concerning a self-consistent statistical treatment of turbulence is that it depends on the flow in which it takes place (for instance wakes, jets or closed flows). At finite Reynolds number, *Re*, most turbulent flows could still keep some average geometrical or topological properties of the laminar flow (for example the presence of a Bénard–von Kármán street in the wake of a bluff body whatever the values of *Re*), which could still influence its statistical properties (Zocchi *et al.* 1994; La Porta *et al.* 2001; Ouellette *et al.* 2006).

Furthermore, we have recently shown for a von Kármán flow that a turbulent flow can exhibit multistability, first-order bifurcations and can even keep traces of its history at very high Reynolds number (Ravelet *et al.* 2004). The observation of this turbulent bifurcation led us to study the transition from the laminar state to turbulence in this inertially driven closed flow.

1.1. *Overview of the von Kármán swirling flow*

1.1.1. *Instabilities of the von Kármán swirling flow between flat disks*

The disk flow is an example where exact Navier–Stokes solutions are available. The original problem of the flow of a viscous fluid over an infinite rotating flat disk was considered by von Kármán (1921). Experimentally, the problem of an infinite disk in an infinite medium is difficult to address. The addition of a second coaxial disk was proposed by Batchelor (1951) and Stewartson (1953). A cylindrical housing can also be added. Instabilities and transitions have been extensively studied in this system for instance Mellor, Chapple & Stokes 1968; Harriott & Brown 1984; Escudier 1984; Sørensen & Christensen 1995; Gelfgat, Bar-Yoseph & Solan 1996; Spohn, Mory & Hopfinger 1998; Gauthier, Gondret & Rabaud 1999; Schouveiler, Le Gal & Chauve 2001; Nore *et al.* 2003, 2004; Nore, Moisy & Quartier 2005). The basic principle of this flow is the following: a layer of fluid is carried near the disk by viscous friction and is thrown outwards by the centrifugal force. By incompressibility of the flow, fluid is pumped toward the centre of the disk. Since the review of Zandbergen & Dijkstra (1987), this family of flow has been called 'von Kármán swirling flow'. In all cases, it deals with the flow between smooth disks, at low Reynolds numbers, enclosed or not in a cylindrical container.

1.1.2. *The 'French washing machine': an inertially driven, highly turbulent von Kármán swirling flow*

Experimentally, the so-called 'French washing-machine' has been a basis for extensive studies of very high-Reynolds-number turbulence in the last decade (Douady, Couder & Brachet 1991; Fauve, Laroche & Castaing 1993; Zocchi *et al.* 1994; Cadot, Douady & Couder 1995; Labbé, Pinton & Fauve 1996; Tabeling *et al.* 1996; Cadot *et al.* 1997; La Porta *et al.* 2001; Moisy *et al.* 2001; Bourgoin *et al.* 2002; Titon & Cadot 2003; Leprovost, Marié & Dubrulle 2004; Marié & Daviaud 2004; Ravelet *et al.* 2004). To reach a Kolmogorov regime in these studies, a von Kármán flow is inertially driven between two disks fitted with blades, at a very high Reynolds number ($10^5 \lesssim Re \lesssim 10^7$). Owing to the inertial stirring, very high turbulence levels can be reached, with fluctuations up to 50% of the blade velocity, as we shall see in this article.

Most of the inertially driven von Kármán setups studied in the past dealt with straight blades. Von Kármán flows with curved-blade impellers were first designed by the VKS-team to study dynamo action in liquid sodium (Bourgoin *et al.* 2002; Monchaux *et al.* 2007). With curved blades, the directions of rotation are no longer equivalent. One sign of the curvature, i.e. with the convex face of the blades forward, direction (+), has been shown to be the most favourable for dynamo action (Marié *et al.* 2003; Ravelet *et al.* 2005; Monchaux *et al.* 2007). The turbulent bifurcation (Ravelet *et al.* 2004) has been obtained with the concave face of the blades forward, direction (−). In this last work, the respective role of the turbulent fluctuations and of the changes in the mean flow with increasing the Reynolds number on the multistability were discussed.

1.2. *Outline of the present article*

Our initial motivation for the present study was thus to obtain an overview of the transition to turbulence and to check the range in which multistability exists. We first describe the experimental setup, the fluid properties and the measurement techniques in § 2. The main data presented in this article are obtained by driving our experiment continuously from laminar to turbulent regimes for this negative direction of rotation, covering a wide range of Reynolds numbers. In § 3 and § 4 we characterize the basic flow and describe the transition from the laminar regime to turbulence through quasi-periodicity and chaos and explore the construction of the temporal spectrum of velocity fluctuations. The continuity and global supercriticality of the transition to turbulence is a main result of this article.

In § 5 we obtain complementary data by comparing the two different directions of rotation and the case with a smooth disk. We show how inertial effects clearly lead to differences for the two directions of rotation at high Reynolds numbers. We then summarize and discuss the main results in § 6.

2. Experimental setup

2.1. *Dimensions, symmetries and control parameter*

The cylinder radius and height are, respectively, $R_c = 100$ mm and $H_c = 500$ mm. A sketch of the experiment is shown in figure 1(*a*). We use bladed disks to ensure inertial stirring. The impellers consist of 185 mm diameter stainless-steel disks each fitted with 16 curved blades, of curvature radius 50 mm and of height $h = 20$ mm (figure 1*b*). The distance between the inner faces of the disks is $H = 180$ mm, which defines a flow volume of aspect ratio $H/R_c = 1.8$. With the curved blades, the directions of rotation are no longer equivalent and we can either rotate the impellers anticlockwise, with the convex face of the blades forward, direction (+), or clockwise, with the concave face of the blades forward, direction (−).

The impellers are driven by two independent brushless 1.8 kW motors, with speed servo-loop control. The maximal torque they can reach is 11.5 N m. The motor rotation frequencies $\{f_1; f_2\}$ can be varied independently in the range $1 \leqslant f \leqslant 15$ Hz. Below 1 Hz, the speed regulation is not efficient, and the dimensional quantities are measured with insufficient accuracy. We will take for exact counter-rotating regimes $f_1 = f_2$ the imposed speed of the impellers f.

The experimental setup is thus axisymmetric and symmetric for rotations of π around any radial axis passing through the centre O ($\mathscr{R}_\pi$-symmetry), and we will consider here only $\mathscr{R}_\pi$-symmetric mean solutions, though mean flows breaking this symmetry do exist for these impellers, at least at very high Reynolds numbers

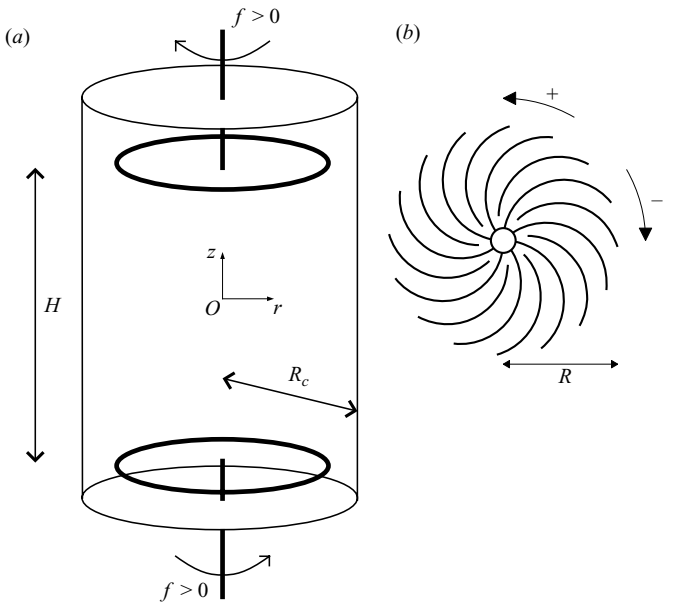

FIGURE 1. (*a*) Sketch of the experiment. The flow volume between the impellers is of height $H = 1.8R_c$. (*b*) Impellers used in this experiment. The disks radius is $R = 0.925R_c$ and they are fitted with 16 curved blades: the two different directions of rotation defined here are not equivalent. This model of impellers has been used in the VKS1 sodium experiment (Bourgoin *et al.* 2002) and is called TM60.

(Ravelet *et al.* 2004). A detailed study of the Reynolds number dependence of the 'global turbulent bifurcation' is outside of the scope of the present article and will be presented elsewhere. Also, since we drive the impellers independently, there is always a tiny difference between f_1 and f_2 and the $\mathscr{R}_\pi$-symmetry of the system cannot be considered as exact. In the following, we will use this symmetry as it is very useful to describe the observed patterns, but we will keep in mind that our system is only an approximation of a $\mathscr{R}_\pi$-symmetric system. The consequences for the dynamics will be analysed in the discussion (§ 6.1).

In the following, all lengths will be expressed in units of R_c. We also use cylindrical coordinates $\{r; z\}$ with origin on the axis of the cylinder and equidistant from the two impellers to take advantage of the $\mathscr{R}_\pi$-symmetry (see figure 1*a*). The time unit is defined using the impeller rotation frequency f. The integral Reynolds number Re is thus defined as $Re = 2\pi f R_c^2 \nu^{-1}$ with ν the kinematic viscosity of the fluid.

As in previous works (Marié & Daviaud 2004; Ravelet *et al.* 2004, 2005), we use water at $20 - 30\,^{\circ}\mathrm{C}$ as working fluid to get Reynolds numbers in the range $6.3 \times 10^4 \lesssim Re \lesssim 1.2 \times 10^6$. To decrease Re down to laminar regimes, i.e. to a few tens, we need a fluid with a kinematic viscosity a thousand times greater than that of water. We thus use 99 %-pure glycerol with kinematic viscosity 0.95×10^{-3} m^2 s^{-1} at $20\,^{\circ}\mathrm{C}$ (Hodgman 1947) and should be able to study the range $50 \lesssim Re \lesssim 900$. To cover a wide range of Reynolds numbers and match these two extreme ranges, we use different mixes of glycerol and water, at temperatures between $15\,^{\circ}\mathrm{C}$ and $35\,^{\circ}\mathrm{C}$. The physical properties of these mixtures are given in table 1, where C is the mass percentage of glycerol in the mixture. Solutions samples are controlled in a Couette viscometer.

C	μ at 15 °C	μ at 30 °C	ρ	Re range
99%	1700	580	1260	50–2000
93%	590	210	1240	130–5600
85%	140	60	1220	550–19000
81%	90	41	1210	840–28000
74%	43	20	1190	1800–56000
0%	1.1	0.8	1000	570000–1200000

TABLE 1. Dynamic viscosity μ (10^{-3} Pa s) at various temperatures, density ρ (kg m^{-3}) at 20 °C and achievable Reynolds number range for various mass concentrations C of glycerol in water.

The temperature of the working fluid is measured with a platinum thermoresistance (Pt100) mounted on the cylinder wall $\{r=1;\ z=0\}$. To control this temperature, thermoregulated water circulates in two heat exchangers placed behind the impellers. Plexiglas disks can be mounted between the impellers and heat exchangers to reduce the flow on the back side of the impellers. They are at typically 50 mm behind the impellers. However, these disks reduce the thermal coupling: they are used in turbulent water flows and removed at low Reynolds number.

2.2. *Experimental tools, dimensionless measured quantities and experimental errors*

Several techniques have been used in parallel: flow visualizations with light sheets and air bubbles, torque measurements and velocity measurements.

Flow visualizations are made in vertical planes illuminated by approximately 2 mm thick light sheets. We look at two different positions in the flow: either the central meridian plane where the radial and axial components are visualized or in a plane almost tangent to the cylinder wall where the azimuthal component dominates. Tiny air bubbles (less than 1 mm diameter) are used as tracing particles.

Torques are measured using the current consumption in the motors given by the servo drives and have been calibrated by calorimetry. Brushless motors are known to generate electromagnetic noise, due to the pulse-width-modulation supply. We use armoured cables and three-phase sinusoidal output filters (Schaffner FN5010-8-99), and the motors are enclosed in Faraday cages, which enhances the quality of the measurements. The minimal torques we measured are above 0.3 N m, and we estimate the error in the measurements to be ± 0.1 N m. The torques T will be presented in the dimensionless form:

$$K_p = T\ \left(\rho R_c^5 (2\pi f)^2\right)^{-1}.$$

Velocity fields are measured by laser Doppler velocimetry (LDV). We use a single-component DANTEC device, with a He–Ne Flowlite Laser (wavelength 632.8 nm) and a BSA57N20 Enhanced Burst Spectrum Analyser. The geometry of the experiment allows us to measure at one point either the axial component $V_z(t)$ or the azimuthal component $V_\theta(t)$. Though the time-averaged velocity field $\boldsymbol{V}$ is not a solution of the Navier–Stokes equations, it is a solenoidal vector field, and it is axisymmetric. We thus use the incompressibility condition $\nabla \cdot \boldsymbol{V} = 0$ to compute the remaining radial component V_r.

The measurements of the time-averaged velocity field are performed on a $\{r \times z\} = 11 \times 17$ grid, weighting velocities by the particles transit time, to remove velocity biases as explained by Buchhave, George & Lumley (1979). This acquisition mode does not have a constant acquisition rate, so we use a different method for the acquisition of well-sampled signals to perform temporal analysis at single points.

In this so-called dead-time mode, we ensure an average data rate of approximately 5 kHz, and the Burst Spectrum Analyser takes one sample every millisecond such that the final data rate is 1 kHz. For practical reasons, this method is well-suited to points close to the cylindrical wall, so we choose the point $\{r = 0.9; z = 0\}$ for the measurements in figures 3, 4 and 5. The signals are re-sampled at 300 Hz by a 'sample and hold' algorithm (Buchhave *et al.* 1979).

Let us now consider the experimental error in the Reynolds number value. The speed servo-loop control ensures a precision of 0.5 % in f, and an absolute precision of ± 0.002 in the relative difference of the impeller speeds $(f_1 - f_2)/(f_1 + f_2)$. The main error in the Reynolds number is thus a systematic error that comes from the estimation of the viscosity. Taking the variation of the viscosity with temperature to be about 4 % for 1°C and the variation with concentration to be about 5 % for 1 % of mass concentration, we estimate the absolute error in Re as ± 10 % (the temperature is known within 1°C). However, the experimental reproducibility of the Reynolds number is much higher than $\pm 10\%$. In the range $100 \lesssim Re \lesssim 500$ we are able to take Re within ± 5.

3. From order to turbulence: description of the regimes

This section describes the evolution of the flow from the laminar regime to the fully developed turbulence, i.e. for $30 \lesssim Re \lesssim 1.2 \times 10^6$. This wide-range study has been carried for the negative sense of rotation (−) of the propellers.

3.1. *Basic state at very low Reynolds number*

At very low Reynolds number, the basic laminar flow respects the symmetries of the problem. It is stationary, axisymmetric and $\mathscr{R}_\pi$-symmetric. This state is stable at $Re = 90$, for which we present a flow visualization in figure 2(*a*, *b*). In figure 2(*a*), the light sheet passes through the axis of the cylinder. The visualized velocities are the radial and axial components. The poloidal part of the flow consists of two toric recirculation cells, with axial pumping directed towards the impellers.

The flow also contains two counter-rotating cells, separated by an azimuthal flat shear layer, which can be seen in figure 2(*b*) where the light sheet is quasi-tangent to the cylinder wall. Both the azimuthal and axial components vanishs in the plane $z = 0$, which is consistent with the axisymmetry and the $\mathscr{R}_\pi$-symmetry. This flat shear layer is sketched in figure 2(*e*). An LDV velocity field is presented in § 5 (figure 10*c*, *d*).

3.2. *First instability – stationary bifurcation*

The first instability for this flow has been determined by visualization and occurs at $Re = 175 \pm 5$ for both directions of rotation. The bifurcation is supercritical, non-hysteretic, and leads to a stationary regime, with an azimuthal modulation of wavenumber $m = 2$. We present a visualization of this secondary state in figure 2(*c*), at $Re = 185$. The axisymmetry is broken: one can see the $m = 2$ modulation of the shear layer, also sketched in figure 2(*e*). Note also that $\mathscr{R}_\pi$-symmetry is partly broken: the bifurcated flow is $\mathscr{R}_\pi$-symmetric with respect to two orthogonal radial axes only. This first instability is very similar to the Kelvin–Helmholtz instability. Nore *et al.* (2003) made a theoretical extension of the Kelvin–Helmholtz instability in a cylinder. Their model is based on the use of local shear-layer thicknesses and Reynolds numbers to take into account the radial variations in the cylindrical case.

We observe this $m = 2$ shear layer to rotate very slowly in a given direction with a period $7500 f^{-1}$. This corresponds to a very low frequency, always smaller than the maximum measured non-symmetry of the speed servo-loop control between the two

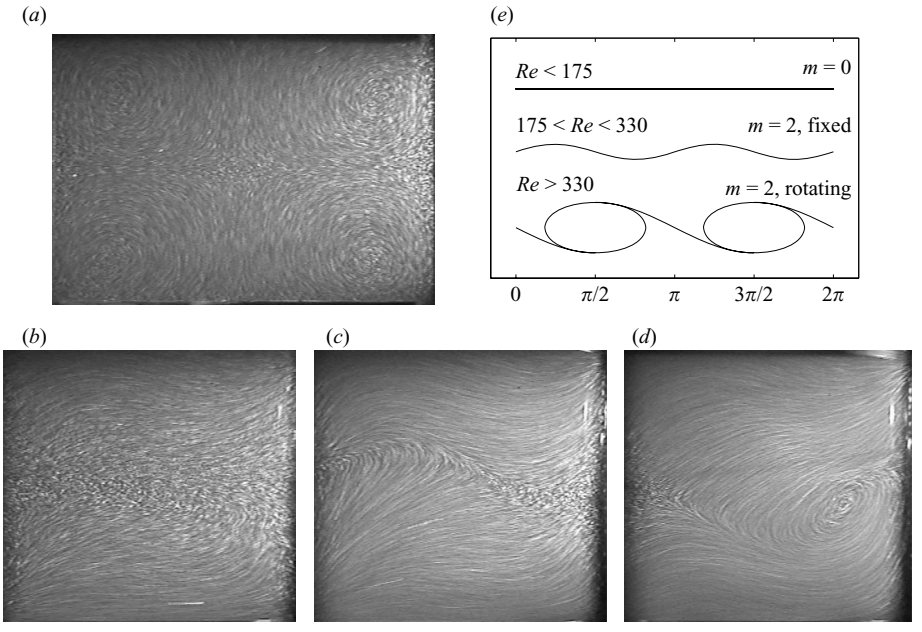

FIGURE 2. Visualization and schematics of the basic laminar flow for impellers rotating in direction (−). The lighting is with a vertical light sheet. Pictures are integrated over 1/25 s with a video camera, and small air bubbles are used as tracers. Picture height is $H - 2h = 1.4R_c$. Laminar axisymmetric flow at $Re = 90$, meridian view (*a*). Views in a plane near the cylinder wall at $Re = 90$ (*b*), $Re = 185$ (*c*) and $Re = 345$ (*d*). The development of the first $m = 2$ instabilities, steady undulation (*c*) and rotating vortices (*d*), is clearly visible in the shape of the shear layer. We give sketches of the shear layer for these Reynolds numbers in (*e*).

independent motors (§ 2.2). This is probably the limit of the symmetry of our system, i.e. the pattern is at rest in the slowly rotating frame where both frequencies are strictly equal (see discussion in § 6.1). For convenience, we will describe the dynamics in this frame.

The laminar $m = 2$ stationary shear-layer pattern is observed up to typically $Re \simeq 300$ where time-dependence arises.

To investigate the time-dependent regimes, we also performed precise velocity measurements at a given point in the shear layer. We measure the azimuthal component v_θ at $\{r = 0.9; z = 0\}$, using the dead-time acquisition mode (see § 2).

Below, we describe and illustrate the dynamics observed and the building-up of the chaotic and turbulent spectra. The next § 4 is complementary: we quantitatively characterize the transitions as far as we can, discuss the mechanisms and finally propose a global supercritical view of the transition to turbulence.

3.3. *From drifting patterns to chaos*

We present time series of the velocity and power spectral densities at five Reynolds numbers in figure 3: $Re = 330 \pm 5$, $Re = 380 \pm 5$, $Re = 399 \pm 5$, $Re = 408 \pm 5$ and $Re = 440 \pm 5$.

3.3.1. *Oscillation at the impeller frequency*

The point at $Re = 330 \pm 5$ is the first at which a clear temporal dynamics is observed: a sharp peak in the spectrum (figure 3*b*) is present at the impeller rotation frequency $f_a = f$, shown enlarged in the inset of figure 3(*a*). This oscillation exists for higher

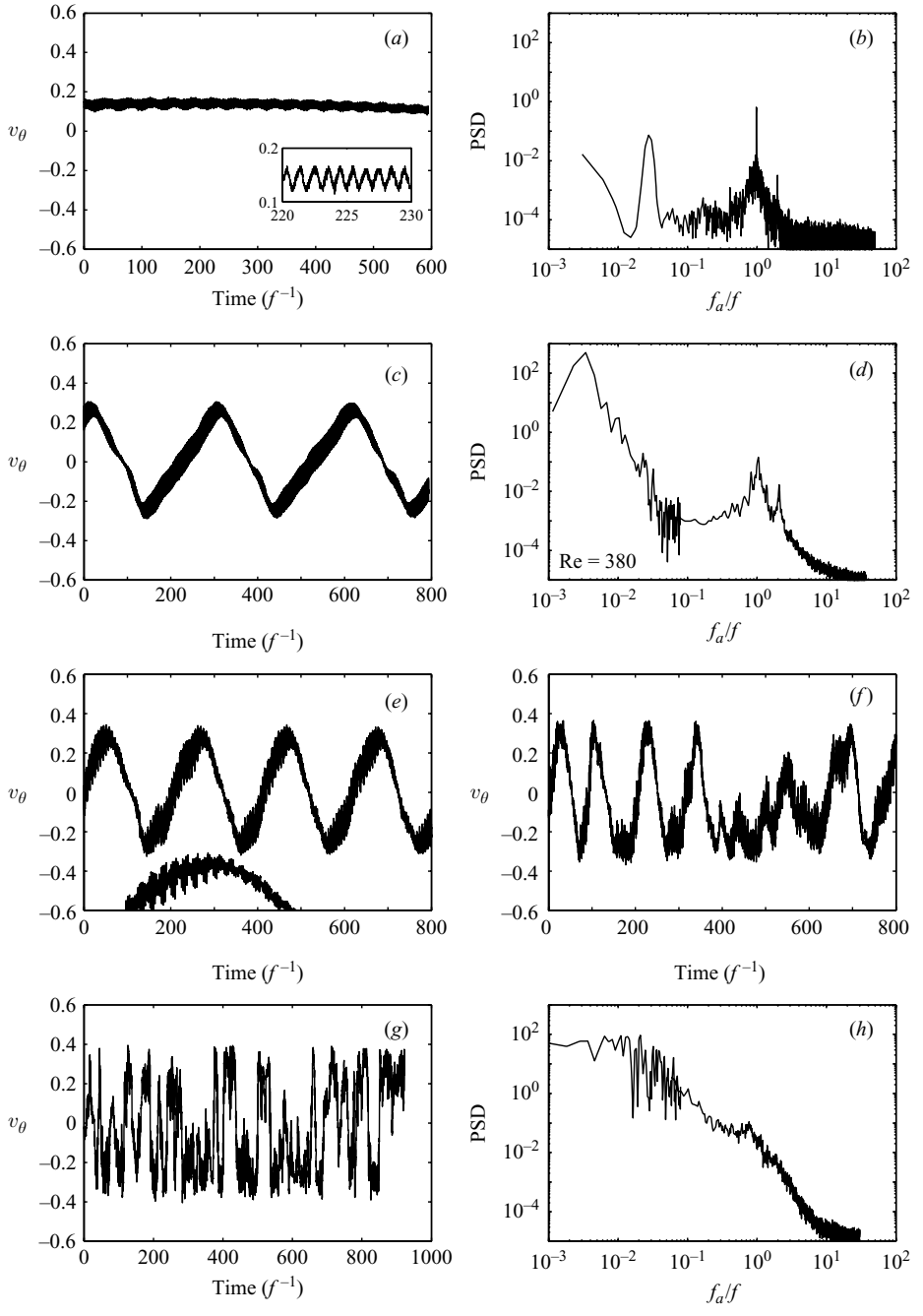

FIGURE 3. Temporal signals $v_\theta(t)$ measured by LDV at $\{r=0.9; z=0\}$ and power spectral densities (PSD), for (a,b) $Re=330$, (c,d) $Re=380$, (e) $Re=399$, (f) $Re=408$ and (g, h) $Re=440$. f_a is the analysis frequency whereas f is the impeller rotation frequency. Inset in (a): zoom of the fast oscillation at frequency f. In (e), a small part of the signal is presented with time magnification ($\times 4$) and arbitrary shift to highlight the modulation at $6.2f^{-1}$. Power spectra are computed by the Welch periodogram method twice: with a very long window to catch the slow temporal dynamics and with a shorter window to reduce fast-scale noise.

Re with the same small amplitude: it is too fast to be visible on the long time series of figure 3, but it is responsible for the large width of the signal line.

In comparison, a similar measurement performed at $Re \simeq 260$ reveals a flat signal with a very low flat spectrum with just a tiny peak, that is 1/1000 of the amplitude measured at $Re = 330$, at $f_a = f$; we have no data between to check the evolution.

On the spectra, we observe the first harmonic, but do not see the expected blade frequency $8f$ nor a multiple of it. So, it is not clear if it corresponds to the basic fluid instability mode or just to a small precessing mode due to the misaligning of the impeller axis or to mechanical vibrations transmitted to the fluid through the bearings. Since the travelling-wave mode of the next section is much stronger and richer in dynamics we will consider that the signal at $f_a = f$ is a 'minor' phenomenon, i.e. a perturbation of the steady $m = 2$ mode.

In figure 3(a) the mean velocity is not zero, but around $v_\theta = +0.17$ during the 600 time units of acquisition, i.e. during 600 disks rotations. This value of the velocity has no special meaning and depends on the phase between the fixed measurement point and the slowly drifting shear layer (§ 3.2). The measurement point stays on the same side of the shear layer for this time series but, on much longer time scales, we measure the typical $m = 2$ shear-layer rotation period.

Further observation of the signal and spectrum of figure 3(a, b) reveals some energy at low frequency around $f_a \simeq f/30$, corresponding to slowly relaxing modulations: the slowness of this relaxation is the clear signature of the proximity of a critical point.

3.3.2. *Drifting/travelling waves*

For $330 < Re < 389$ the velocity signal is periodic with a low frequency f_D. This is illustrated at $Re = 380$ in figure 3(c, d). The mean velocity is now zero: the shear layer rotates slowly such that the measurement point is alternately in the cell rotating with the upper impeller ($v_\theta > 0$) and in the cell rotating with the lower impeller ($v_\theta < 0$). Visualizations confirm that this corresponds to a travelling wave (TW) or a drifting pattern and also show that the $m = 2$ shear layer is now composed of two vortices (figure 2d) and thus merits the name 'mixing-layer'. Along the equatorial line, the parity is broken or the vortices are tilted (Coullet & Iooss 1990; Knobloch 1996). The velocity varies between $-0.3 \lesssim v_\theta \lesssim 0.3$. The drift is still slow but one order of magnitude faster than the drift described above for the 'steady' $m = 2$ pattern: one can see two periods during 600 time units, i.e. $f_D = f/300$, which is very difficult to resolve by spectral analysis owing to the shortness of the signal (see the caption of figure 3). At $Re = 380$ (figure 3c, d), the peak at the rotation frequency is still present, but starts to spread and becomes broadband. The power spectral density at frequencies higher than $3f$ decreases extremely rapidly to the noise level. Note that the $\mathscr{R}_\pi$-symmetry remains only with respect to a pair of orthogonal radial axes which rotates with the propagating wave.

3.3.3. *Modulated travelling waves*

For $389 < Re < 408$ the signal reveals quasi-periodicity, i.e. modulated travelling waves (MTW), shown in figure 3(e, f) at $Re = 399$ and 408. The MTW are regular, i.e. strictly quasi-periodic below $Re = 400$ and irregular above. The modulation frequency (see the magnified ($\times 4$) part of the signal in figure 3e) is $f_M = f/(6.2 \pm 0.2)$ whatever Re, even above $Re = 400$. It is much faster than the drift frequency ($f_D \sim f/200$) and movies show that it seems to be related to oscillations of the mixing-layer vortex cores.

3.3.4. *Chaotic regime*

The upper limit of the regular dynamics is precisely and reproducibly $Re = 400$ and there is no hysteresis. From the visualizations, we observe that the $m = 2$ symmetry is now broken. The mixing-layer vortices, which are still globally rotating around the cell in the same direction, also behave more and more erratically with increasing Re: their individual dynamics includes excursions in the opposite direction as well as towards one or other impeller. The velocity signal also loses its regularity (see figure 3*e–g*).

When this disordered regime is well established, *e.g.* for $Re = 440$ (figure 3*g*), it can be described as series of almost random and fast jumps from one side to the other of the $v = 0$ axis. The peaks reached by the velocity are now in the range $-0.4 \lesssim v_\theta \lesssim 0.4$. The spectral analysis of the signal at $Re = 440$ (figure 3*h*) no longer reveals any well-defined frequency peaks. However, a continuum of highly energetic fluctuations at low frequency, below $f_a = f$ and down to $f_a = f/100$, emerges. A small bump at the rotation frequency f is still visible, and a region of fast fluctuations above the injection frequency also arises. Although we did not carried detailed Poincaré analysis or equivalent and cannot clearly characterize a scenario, we find this transition and this regime typical enough to call it 'chaos' (see also § 4.2).

3.4. *From chaos to turbulence: building a continuous spectrum*

Increasing the Reynolds number further, one obtains the situation depicted in figure 4. The time spectrum is now continuous but still evolving. We describe the situations below and above the impeller frequency f separately.

3.4.1. *Slow time scales*

The slow dynamics which has already been described at $Re = 440$ (figure 3*g*, *h*) could be thought to depend only on the largest spatial scales of the flow. It is well established above $Re \simeq 10^3$ (figure 3*b*). The mean velocities corresponding to each side of the mixing layer are of the order of ± 0.6 at $Re = 1.0 \times 10^3$ and above (figure 4*a*, *c*, *g*). The power spectral density below the injection frequency seems to follow a f^{-1} power law over two decades (see discussion § 6.2) for all these Reynolds numbers (figure 4). The spectral density saturates below $10^{-2} f$.

3.4.2. *Fast time scales*

However, the fast time scales, usually interpreted as a trace of fluctuations of small spatial scales evolve between $Re = 1.0 \times 10^3$ and $Re = 6.5 \times 10^3$. At the former Reynolds number, there are few fast fluctuations decaying much faster than $f^{-5/3}$ (figure 4*b*) and the intermittent changeovers are easy to identify in the temporal signal in figure 4(*a*). If the Reynolds number is increased, the fast (small-scale) fluctuations get increasingly bigger and follow a power law over a growing frequency range (figure 4*e*, *f*, *h*). The measured slope is of order of -1.55 over 1.5 decade, i.e. 10% lower than the classical $f^{-5/3}$. This value of the exponent could be ascribed to the so-called 'bottleneck' effect (Falkovich 1994) and is compatible with the values given by Lohse & Müller-Groeling (1995) (-1.56 ± 0.01) for a Taylor-microscale Reynolds number $R_\lambda \simeq 100$, which is an estimation for our flow based on the results of Zocchi *et al.* (1994).

4. Quantitative characterization of the transitions

The various dynamic states encountered have been described and illustrated in the previous section. Now, we wish to analyse some characteristic measurements, i.e. the

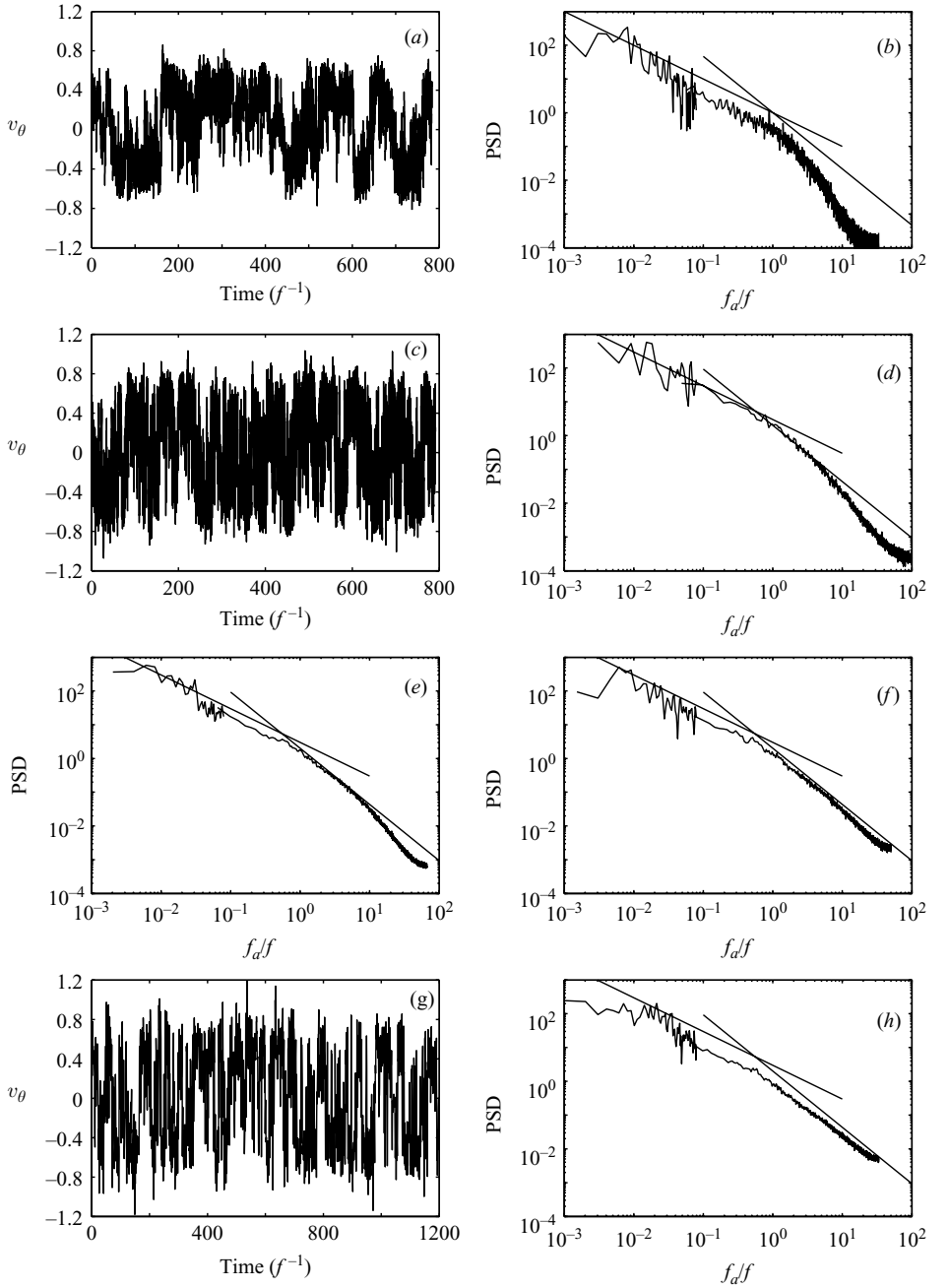

FIGURE 4. (a, b) Temporal signal $v_\theta(t)$ measured by LDV at $\{r = 0.9; z = 0\}$ and power spectral density at $Re = 1.0 \times 10^3$. (c, d) Temporal signal and power spectral density at $Re = 1.7 \times 10^3$. (e, f) Power spectral densities at 2.7×10^3 and 3.8×10^3. (g, h) Temporal signal and power spectral density at 6.5×10^3. Solid lines in the power spectra plots are power-law eye-guides of slope -1 and $-5/3$. Spectra are computed as explained in the caption of figure 3.

amplitude of the velocity fluctuations and their main frequencies, extract thresholds and critical behaviours and then address the question of the nature of the reported transitions.

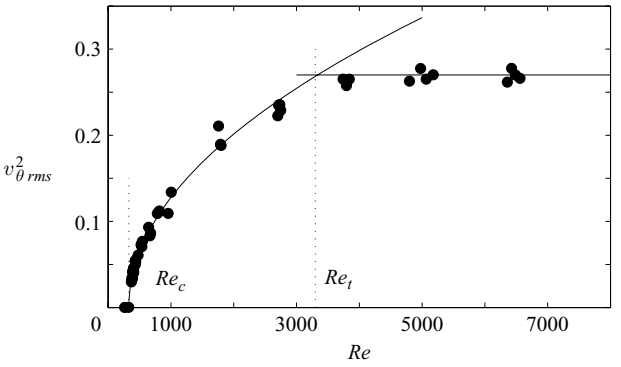

FIGURE 5. Variance of $v_\theta(t)$ measured at $\{r=0.9; z=0\}$ *vs.* Re. Solid curve: nonlinear fit of the form $v^2_{\theta\ rms} = a \times (Re - Re_c)^{1/2}$, fitted between $Re = 350$ and $Re = 2500$. The regression coefficient is $R^2 = 0.990$, and the fit gives $Re_c = 328 \pm 8$ with 95 % confidence interval. The intersection between this fit and the asymptotic value $v^2_{\theta\ rms} \simeq 0.27$ gives $Re_t = 3.3 \times 10^3$.

4.1. *From order to turbulence: a global supercriticality*

It is known that fully turbulent von Kármán flow can generate velocity fluctuations of typically 50 % of the driving impeller velocity. So, we compute the variance $v^2_{\theta\ rms}$ of the LDV time series *versus* the Reynolds number. This quantity is equivalent to a kinetic energy and can be referred to as the azimuthal kinetic energy fluctuations in the mixing layer. With this method, we consider the broadband frequency response of the signal. The results are reported in figure 5 for all the measurements performed between $260 \lesssim Re \lesssim 6500$. Except at the time-dependence threshold, this quantity behaves smoothly: it can be fitted between $Re = 350$ and $Re = 2500$ with a law in the square root of the distance to a threshold $Re_c \simeq 330$ (figure 5):

$$v^2_{\theta\ rms} \propto (Re - Re_c)^{1/2}.$$

Since we will show below that Re_c is precisely the threshold for time-dependence, we can make the hypothesis that $v^2_{\theta\ rms}$ is a global order parameter for the transition to turbulence, i.e. for the transition from steady flow to turbulent flow taken as a whole. With this point of view the transition is globally supercritical.

4.2. *Transitions from order to chaos*

We now turn to the first steps in the transition to time dependence. We monitor the main frequencies of the mixing-layer dynamics in the TW- and MTW-regimes (see § 3.3). In these regimes, even though only a few periods are monitored along single time-series, we carefully estimate the period by measuring the time delay between crossings of the $v = 0$ axis. These values are shown in figure 6(a) with circles. In an equivalent way, the periodicity of the travelling of the mixing-layer vortices on the visualizations give complementary data, represented by squares on the same figure.

4.2.1. *Onset of time-dependence*

The drift frequency f_D of the travelling waves behaves linearly with Re above a threshold Re_{TW} very close to 330. Both measurement methods agree though as the visualizations have large error bars in Re due to the shortness of our records and to a poorer thermal control, the fit is made on velocity data only. We observe some imperfection in the quasi-periodic bifurcation, due to the pre-existing slow drift below

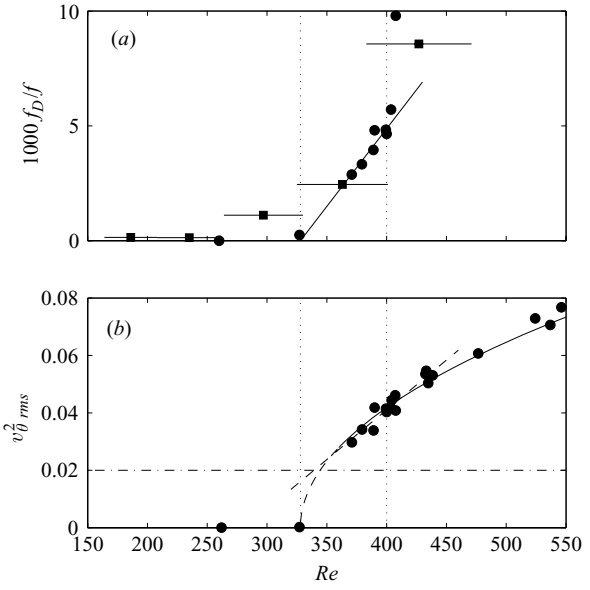

FIGURE 6. (*a*) Low-frequency f_D of the quasi-periodic regime of velocity $v_\theta(t)$ measured at $\{r=0.9; z=0\}$ (circles) and drift frequency of the $m=2$ shear-layer pattern from flow visualizations (squares with large horizontal error bars due to poorer temperature control). The solid line is a linear fit of f_D between the two thresholds $Re_{TW}=330$ and $Re_{chaos}=400$, indicated by vertical dotted lines. (*b*) Enlargement of figure 5. The dashed line is a linear fit of the lowest data between $Re=350$ and $Re=450$. Close to the threshold, it crosses the dash-dotted line which corresponds to the velocity due to the drift and estimates the level of imperfection.

Re_{TW}: we always observe the mixing layer to start rotating in the sense of the initial drift.

We show in figure 6(*b*) an enlargement of figure 5, i.e. the amplitude of the kinetic energy fluctuations. We observe that both the quadratic amplitude fit and the linear frequency fit converge to exactly the same threshold $Re_{TW}=Re_c=328$. We can conclude that the low-frequency mode at $f_a=f_D$ bifurcates at $Re=330\pm5$ through a zero-frequency bifurcation for f_D.

The question is thus precisely how the amplitude behaves at onset. There is obviously a lack of data in the narrow range $300\lesssim Re\lesssim350$ (figure 6*b*). It is due to the high temperature dependence of the viscosity in this regime (Reynolds number varied quite fast even with thermal control) and to some data loss at the time of the experimental runs. Despite this lack, we present these observations because of the consistency of the different types of data – visualizations, LDV, torques – over the wide Reynolds number range. The horizontal line $v_{\theta\ rms}^2=0.02$ in figure 6(*b*) corresponds to an amplitude of typically 0.15 for v_θ, which is produced just by the initial shear-layer drift (see the maximum speed in figure 3*a*). This value is in good agreement with a linear extrapolation over the lower range of figure 6(*b*) and thus again with an imperfect bifurcation due to the drift. If we reduce the drift by better motor frequencies matching, the onset value of v_θ will depend on the height of the probe location and the parabola of figure 6(*b*) could perhaps be observed on the $m=2$ shear-layer modes.

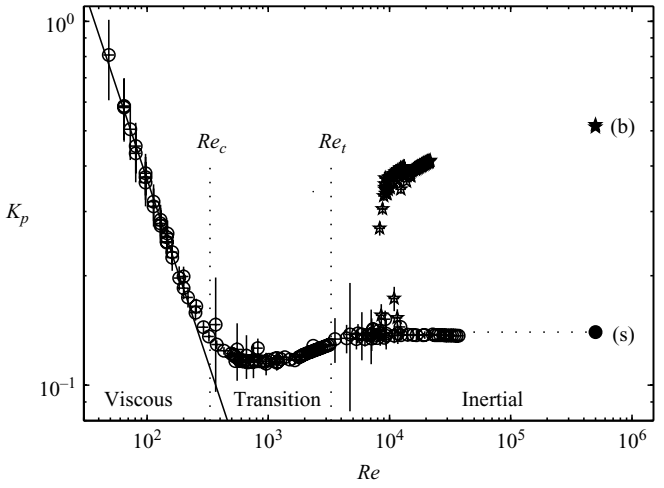

FIGURE 7. Dimensionless torque K_p *vs.* Re in a log-log scale for the negative sense of rotation (−) of the impellers. The main data (○) correspond to the symmetric (s)-flow regime described here. For completeness, the high-torque branch (⋆) for $Re \gtrsim 10^4$ corresponds to the (b) flow regime (Ravelet *et al.* 2004), i.e. to the 'turbulent bifurcation' (see § 4.4). Since the two motors do not deliver the same torque in this $\mathscr{R}_\pi$-symmetry-broken (b) flow, the average of both values is plotted. Relative error in Re is $\pm 10\,\%$; absolute error of ± 0.1 N m in the torque. Re_c and Re_t are the transition values computed from the fits of figure 5. The single points displayed at $Re = 5 \times 10^5$ correspond to measurements in water, where K_p is extracted from a fit of the dimensional torque by $a + b \times f^2$ for $2 \times 10^5 \lesssim Re \lesssim 9 \times 10^5$ (Ravelet *et al.* 2005).

4.2.2. *Transition to chaos*

The very sharp transition to chaos is observed for $Re > Re_{chaos} = 400$. There is no hysteresis. Just above the chaotic threshold in the MTW regime (figure 3*f*), the signal sometimes exhibits a few almost-quasi-periodic oscillations, still allowing us to measure a characteristic frequency. The measured values have also been plotted on figure 6(*a*) and are clearly above the linear fit. This could reveal a vanishing time scale, i.e. a precursor for the very sharp positive/negative jumps of v_θ reported in the chaotic and turbulent regimes.

We do not clearly observe any evidence of mode locking between the present frequencies which are in the progression $f/200 \to f/6.2 \to f$ and there is no trace of a sub-harmonic cascade on any of each. This could be linked to a three-frequency scenario like Ruelle–Takens (Manneville 1990).

4.3. *Transition to full turbulence*

4.3.1. *Torque data*

Complementary to the local velocity data, information can be collected on spatially integrated energetic data, i.e. on torque measurements $K_p(Re)$ (figure 7). The low-Reynolds-numbers viscous part will be described below (§ 5) as well as the high-torque bifurcated branch (§ 4.4). In the high-Reynolds-number regimes, the torque reaches an absolute minimum for $Re \simeq 1000$ and becomes independent of Re above 3300.

4.3.2. *From chaos to turbulence*

Is there a way to quantitatively characterize the transition or the crossover between chaos and turbulence? These seems to be no evidence of any special sign to indicate the change between the two regimes. A possible empirical criterion would be the

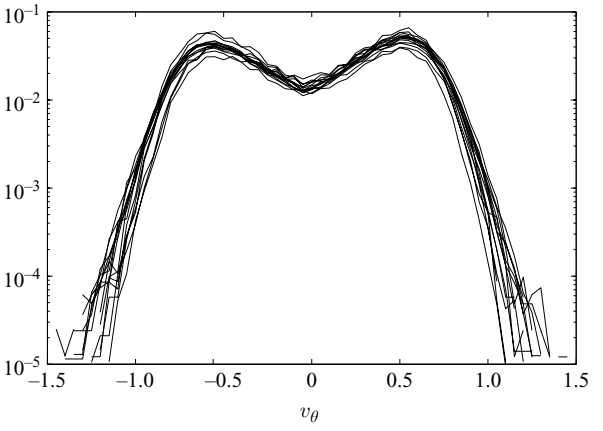

FIGURE 8. Probability density function (PDF) of v_θ for 16 Reynolds numbers in the range $2.5 \times 10^3 \lesssim Re \lesssim 6.5 \times 10^3$.

completeness of the $(f_a/f)^{-1}$ low-frequency part of the spectrum, clearly achieved for $Re = 1000$ (figure 4*b*). This region also corresponds to the minimum of the $K_p(Re)$ curve (figure 7). One could propose that below this Reynolds number, the power injected at the impeller rotation frequency mainly excites low frequencies belonging to the 'chaotic' spectrum, whereas above $Re \simeq 1000$ it also drives the high frequencies through the Kolmogorov–Richardson energy cascade.

4.3.3. *Inertial turbulence*

The $(Re - Re_c)^{1/2}$ behaviour can be fitted through the quasi-periodic and chaotic regimes, up to $Re \sim 3000$. Here, the azimuthal kinetic energy fluctuation level saturates at $v_{\theta\ rms}^2 \simeq 0.27$, i.e. fluctuations of velocities at this point of the mixing layer are of the order of 50 % of the impeller tip speed. This saturation is also revealed by the probability density functions (PDFs) of v_θ presented in figure 8. These PDFs are computed for 16 Reynolds numbers in the range $2.5 \times 10^3 \lesssim Re \lesssim 6.5 \times 10^3$. Note the bimodal character of the PDFs: the two bumps, which are symmetric, correspond to the two counter-rotating cells. Furthermore, all these PDFs collapse and are therefore almost independent of Re in this range. This is also consistent with the spectral data of figure 4(*b–d*) where the $(f_a/f)^{-1}$ slowest time-scale regions which contain most of the energy, below f, appear similar for $Re = 1.0 \times 10^3$ and above (figure 4). The crossover Reynolds number Re_t at which the kinetic energy of fluctuations saturates in figure 5 is estimated by taking the intersection of the horizontal asymptote with the fit: $Re_t = 3.3 \times 10^3$. This value corresponds precisely to the value at which the asymptotic plateau is reached in the K_p *vs. Re* diagram (figure 7). In such an inertially driven turbulent flow, the bulk dissipation is much stronger than the dissipation in boundary layers and the global dimensionless quantities thus do not depend on the Reynolds number past a turbulent threshold (Lathrop, Fineberg & Swinney 1992; Cadot *et al.* 1997).

4.4. *Higher Reynolds number: multistability and turbulent bifurcation*

From all the observations reported above in the negative direction of rotation, we conclude that the transition to turbulence is completed at Re_t and that the azimuthal kinetic energy fluctuation can be considered as an order parameter for the global

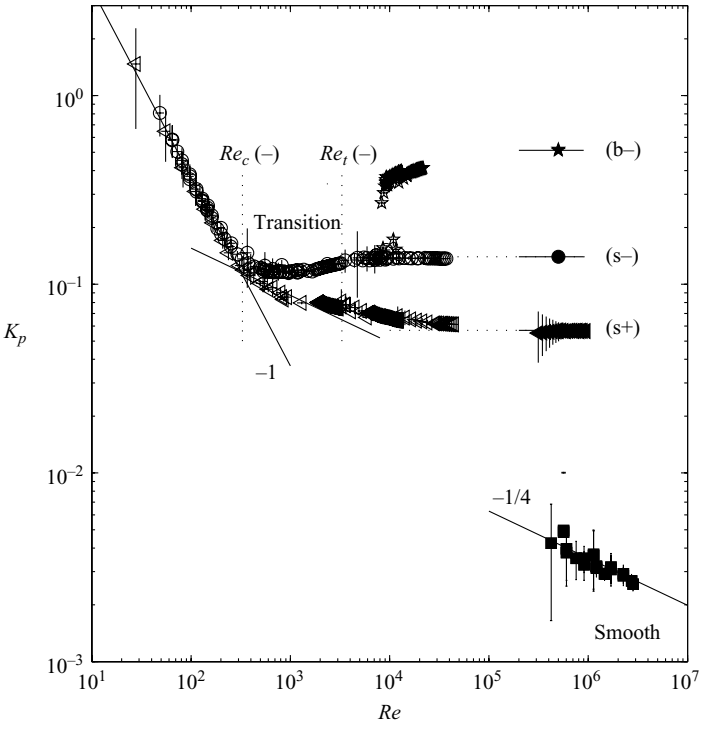

FIGURE 9. Compilation of the dimensionless torque K_p *vs.* Re for various flows. All data are for $\mathscr{R}_\pi$-symmetric von Kármán flows except the branch labelled (b−) ($\star$): see caption of figure 7 for details. $\circ$, direction of rotation (−); $\triangle$ direction of rotation (+); the solid line is a nonlinear fit of equation $K_p = 36.9 \times Re^{-1}$ between $Re = 30$ and $Re = 250$. Some data for flat disks of standard machine-shop roughness, operated in pure water up to 25 Hz (squares) are also displayed with a $Re^{-1/4}$ fit. A $-1/4$ power law is fitted for the positive direction of rotation for $330 \leqslant Re \leqslant 1500$ and is displayed between $Re = 10^2$ and $Re = 10^4$. Relative error in Re is $\pm 10\,\%$; absolute error of ± 0.1 N m on the torque. Re_c and Re_t are the transition values computed from the fits of figure 5.

transition, from the onset of time-dependence $Re_c = 330$ to the fully turbulent state transition/crossover at $Re_t = 3.3 \times 10^3$, i.e. over a decade in Reynolds number.

In the inertial regime above Re_t, the von Kármán flow driven by high-curvature bladed impellers rotating in the negative direction presents another original behaviour: Ravelet *et al.* (2004) have shown that the turbulent von Kármán flow can exhibit multistability at high Reynolds number. To study and analyse this phenomenon, it is necessary to introduce an additional parameter: the rotation velocity difference $\Delta f = f_2 - f_1$ between the two impellers. The so-called 'turbulent bifurcation' and multistability are observed exclusively for the negative direction of rotation. So, the $\Delta f = 0$ regime presented here, called (s) for symmetric in Ravelet *et al.* (2004), can be observed only if both motors are started together, i.e. if Δf is kept equal to zero at any time. Once a velocity difference is applied for long enough, depending of the magnitude of $|\Delta f|$, the flow changes abruptly to a one-cell-flow with axial pumping towards one of the impellers only instead of towards each impeller. This new flow, called (b) for bifurcated in Ravelet *et al.* (2004), strongly breaks the $\mathscr{R}_\pi$-symmetry, has no middle shear layer and requires much higher torque from the motors: typically 3 times the value of (s)-flow, with a finite difference between the two motors. The

mean reduced torque at $\Delta f = 0$ is plotted with stars in figure 7: branches (s) and (b) co-exist for $Re \gtrsim Re_m = 10^4$. To recover the $\mathscr{R}_\pi$-symmetric flow, one should stop the motors or at least decrease Re below Re_m.

Note that this multistability is only observed above Re_t, i.e. for flows with a well-developed turbulent inertial Kolmogorov cascade. Furthermore, cycles in the parameter plane $\{K_{p2} - K_{p1};\ f_2 - f_1\}$ have been made for various Re between 100 and 3×10^5 (Ravelet 2005). At low Reynolds numbers, $Re \lesssim 800$, this cycle is reduced to a continuous, monotonic and reversible line in the parameter plane. The first appearance of 'topological' transformations of this simple line into multiple discontinuous branches of a more complex cycle is seen at $Re \simeq 5 \times 10^3$, in the neighbourhood of the transitional Reynolds number Re_t, and multistability for $\Delta f = 0$ is first observed for $Re \sim 10^4$. The extensive study of this turbulent bifurcation with varying Re deserves separate treatment and will be reported elsewhere.

From the above preliminary report of our results, we emphasize that the turbulent bifurcation seems specific to fully developed turbulent flows. Whereas the exact counter-rotating flow ($\Delta f = 0$) will never bifurcate (Ravelet *et al.* 2004), for a small Δf $(0 < |\Delta f|/f \ll 1)$ this turbulent bifurcation around $Re_m = 10^4$ will correspond to a first-order transition on the way to infinite-Reynolds-number dynamics: this flow appears an ideal prototype of an ideal system undergoing a succession of well-defined transitions from order to high-Reynolds-number turbulence.

4.5. *The regimes: a summary*

The next section concerns some aspects specific to the inertial stirring. Then follows a discussion (§ 6) about the role of the symmetries and of the spatial scales of the flow which can be read almost independently. The following summary of the observed regimes and transitions is given to support the discussion.

$Re < 175$: $m = 0$, axisymmetric, $\mathscr{R}_\pi$-symmetric steady basic flow (§ 3.1),
$175 < Re < 330$: $m = 2$, discretely $\mathscr{R}_\pi$-symmetric steady flow (§ 3.2),
$330 < Re < 389$: $m = 2$, non $\mathscr{R}_\pi$-symmetric, equatorial-parity-broken travelling waves (§ 3.3.2, § 4.2.1),
$389 < Re < 400$: modulated travelling waves (§ 3.3.3),
$400 < Re < 408$: chaotic modulated travelling waves (§ 3.3.3),
$400 < Re \lesssim 1000$: chaotic flow (§ 3.3.4, § 4.2.2),
$1000 \lesssim Re \lesssim 3300$: transition to turbulence (§ 3.4, § 4.3.2),
$Re \gtrsim 3300$: inertially driven fully turbulent flow (§ 4.3.3),
$Re \gtrsim 10^4$: multivalued inertial turbulence regimes (§ 4.4).

5. Viscous stirring vs. inertial stirring

We now focus on the details of the inertial stirring. So for, a single rotation sense, the negative (−), has been studied. However, relevant information can be obtained from the comparison of data from both senses of impellers rotation, which is equivalent to having two sets of impellers with opposite curvature at any time in the same experiment.

The guideline for this analysis is the global energetic measurements over the whole Reynolds number range. The data for sense (−) have already been partly discussed above (figure 7), but the full set is shown here in figure 9. At low Reynolds number the two curves are identical, which means that the blades have no effect on the viscous stirring. This is analysed in § 5.1. However, at high Reynolds number, there is a factor

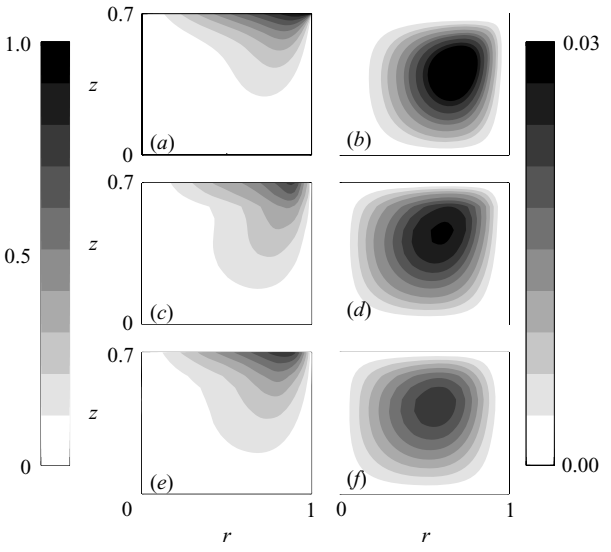

FIGURE 10. Comparison between a numerical simulation (a, b) performed with the code of Nore *et al.* (2003) in a cylinder of aspect ratio $\Gamma = 1.4$ at $Re = 120$ and two experimental velocity fields measured by LDV in direction (+) at $Re = 130$ (c, d) and in direction (−) at $Re = 120$ (e, f). The flow quantities which we present are in (a, c, e) the azimuthal velocity v_θ and in (b, d, f) the poloidal stream function Ψ. Presenting the fields between $0 \leqslant r \leqslant 1$ and $0 \leqslant z \leqslant 0.7$ is sufficient due to axisymmetry and $\mathscr{R}_\pi$-symmetry. Blades or smooth disk are at $z = 0.7$.

3 between the two curves, denoting very different inertial regimes, as discussed in § 5.2.

5.1. *From viscous to inertial stirring*

While $Re \lesssim 300$, the dimensionless torque K_p scales as Re^{-1}. We are in the laminar regime (Schlichting 1979) and the viscous terms are dominant in the momentum balance. These regimes correspond to $m = 0$ or $m = 2$ steady flows, with an eventual slow drift (§§ 3.1 and 3.2).

From the power consumption point of view, both directions of rotations are equivalent. The two curves – circles for direction (−) and left-pointing triangles for direction (+) – collapse for $Re \lesssim 300$ onto a single curve with equation $K_p = 36.9 Re^{-1}$.

We performed velocity field measurements for the two flows at $Re \simeq 120$–130 (figure 10c–f). The differences between the two directions are minor. The order of magnitude of the mean poloidal and toroidal velocities are the same to within 15 % for both directions of rotation in the laminar regime, whereas at very high Re, they strongly differ (by a factor 2) (Ravelet *et al.* 2005).

The flow is thus not sensitive to the shape of the impeller blades in the laminar regime. To explain this, we make the hypothesis that for these large impellers of radius $0.925 R_c$, fitted with blades of height $h = 0.2 R_c$, the flow at low Re is equivalent to the flow between flat disks with an effective aspect ratio $\Gamma = (H - 2h)/R_c = 1.4$. Nore *et al.* (2004) numerically studied the flow between counter-rotating smooth flat disks enclosed in a cylinder and report the dependence of the first unstable mode wavenumber on the aspect ratio $\Gamma = H/R_c$. In their computations, the critical wavenumber is $m = 1$ for $\Gamma = 1.8$, whereas for $\Gamma = 1.4$, it is $m = 2$ as we observe in our experiments.

We thus compare in figure 10 our experimental velocity fields to a numerical simulation performed by Caroline Nore (personal communication) at the same Re and aspect ratio $\Gamma = 1.4$. The three fields are very close. A possible physical explanation for this effect is the presence of viscous boundary layers along the resting cylinder wall. The typical length scale of the boundary layer thickness can be estimated as $\delta = Re^{-1/2}$. At the Reynolds number at which the impellers blades start to have an effect, i.e. at $Re \simeq 300$, this boundary layer thickness is of the order of $\delta \simeq 6$ mm, while the gap between the impellers and the cylinder wall is 7.5 mm. It is also of the order of magnitude of the minimum distance between two blades. For $Re \lesssim 300$, the fluid is thus kept between the blades and cannot be expelled radially: it rotates with the impellers. The stirring cannot be considered as inertial and does not depend on the blade shape.

For $Re \gtrsim 300$, the dimensionless torque starts to shift from a Re^{-1} law and simultaneously there is a difference between the two senses of rotation: the inertial stirring becomes dominant over the viscous stirring. Simultaneously, the steady flow becomes unstable with respect to time-dependence (§§ 3 and 4).

5.2. *Inertial effects*

At high Reynolds number, we observe in figure 9 different behaviours for K_p for the two senses of rotation. Sense (−) passes through a minimum for $Re \simeq 1000$ and then rapidly reaches a flat plateau above $Re_t = 3300$ (see § 4.3), whereas sense (+) asymptotically reaches a regime with only a third of the power dissipation of sense (−). Together with the curved-blade data, figure 9 presents additional data for smooth disks. The dimensionless torque K_p is approximately 30 times smaller for smooth disks than for curved-bladed disks, and does not display any plateaux at high Reynolds number but a $Re^{-1/4}$ scaling law, as described by Cadot *et al.* (1997).

It is tempting to compare our curve $K_p(Re)$ with the classical work of Nikuradse (1932, 1933) consisting of a complete and careful experimental data set on the turbulence in a pipe flow with controlled wall roughness. The data concern the friction factor, equivalent to K_p, measured over a wide range between $Re = 500$ and $Re = 10^6$, which is shown to strongly depend on the wall roughness above $Re \simeq 3000$. The wall roughness is made up of controlled sand grains of diameter in the range $1/507$ to $1/15$ of the pipe radius, somewhat smaller than our blade height $h/R_c = 1/5$ which can be thought of as an effective roughness.

This data set has defied theoretical interpretation for decades and still motivates papers. Recently, Goldenfeld (2006) and Gioia & Chakraborty (2006) proposed phenomenological interpretations and empirical reduction of Nikuradse's data. In brief, both connect the very high-Reynolds-number inertial behaviour – a plateau at a value which scales with the roughness to the power $1/3$ – to the Blasius $Re^{-1/4}$ law for the dissipative region at intermediate Re. Goldenfeld (2006), using a method from critical-point physics, finds a scaling for the whole domain above $Re \simeq 3000$, whereas Gioia & Chakraborty (2006) describe the friction factor over the same Reynolds number range according to Kolmogorov's phenomenological model.

Compared with pipe flow results and models, our $K_p(Re)$-curve (figure 9) looks very similar except for the region Gioia & Chakraborty (2006) called the energetic regime. Indeed, in our specific case the basic flow is already dominated by vortices of the size of the vessel. The negative direction (circles in figure 9) shows a minimum followed by a plateau above $Re_t = 3300$ and is in agreement with the general inertial behaviour described above. However for the positive direction (left-pointing triangles

in figure 9), the K_p curve seems to be continuously decreasing up to $Re \simeq 10^6$. Looking closer, one can observe a short $Re^{-1/4}$ Blasius regime for Re between 300 and 1500, highlighted by a fit in figure 9, followed by a very slow variation over the next two decades: logarithmic corrections are still visible in the range $10^4 \lesssim Re \lesssim 5 \times 10^4$. For this direction it is more difficult to define a threshold for the plateau observed in pure water (Marié 2003). Nevertheless, this threshold should be of order 10^5, i.e. much higher than with negative rotation.

A possible explanation of this strong difference may lie in the structure of the flow inside the impellers, i.e. between the blades. Let us first assume that this flow is dominated by what happens along the extremities of the blades, on which the pressure is higher. Then we assume that the blade curvature leads to stable boundary layers in positive rotation and to Görtler instability in negative rotation. The former develops Blasius boundary layers, whereas the latter develops turbulent boundary layers with many more vortices. Therefore, when the boundary layer detaches, somewhere along the blades or at least at their end, the Blasius boundary layer in the positive rotation sheds fewer turbulent vortices than the Görtler unstable layer does in the negative rotation.

The above description could be sufficient to explain why the negative rotation is able to produce a Kolmogorov cascade even at quite low Reynolds numbers near Re_t. However if, in the positive rotation case, the flow is only seeded by vortices produced by the stable boundary layer which develops along the smooth blade faces, it is clear that a Blasius $Re^{-1/4}$ regime could be observed in this transition Reynolds range and that a full inertial regime does not occur below a very high Reynolds number owing to the very small roughness of the blade faces. This could be why the two curves in figure 9 look so different: the lower one looks qualitatively like a low-roughness boundary flow and the upper one like a high-roughness boundary flow. However, this may only account for part of the flow driving: the resistive torque is much higher for bladed impellers than for flat disks as shown in figure 9.

Our observation of the closed von Kármán turbulent flow is thus consistent with the claim by Goldenfeld (2006) that full understanding of turbulence requires explicit accounting for boundary roughness.

6. Discussion and conclusion

6.1. *Symmetries and first bifurcations*

As for many flows, the similarity of the flow behaviour at low Reynolds number with an intermediate-size nonlinear system is obvious: breaking of spatial symmetry first, then a temporal symmetry and finally transition to chaos by a quasi-periodic scenario.

A comparable study has been carried both experimentally and numerically on von Kármán flow with flat disk and variable aspect ratio by Nore *et al.* (2003, 2004, 2005). Our results agree well with their results on the first instability mode $m = 2$ if considering the fluid in the blade region as in almost solid-body motion, which reduces the aspect ratio (see § 5.1). However, all thresholds appear at much lower Re for bladed impellers than for flat disks: 175 *vs.* 300 for the first steady bifurcation and 330 *vs.* above 600 for the first temporal instability of the $m = 2$ mode, not observed in Nore *et al.* (2005) study.

Another important difference between the two systems concerns symmetries. Whereas Nore and collaborators deal with exact counter-rotation by using a single

motor to drive both disks, our experimental setup uses two independent motors and reaches only an approximation of a counter-rotating regime. As a consequence, the $\mathscr{R}_\pi$-symmetry is *stricto sensu* broken at any Reynolds number and the symmetry group of our problem is $SO(2)$ instead of $O(2)$. To evaluate the level of symmetry breaking we can use a small parameter (Chossat 1993; Porter & Knobloch 2005), e.g. $\epsilon = (f_1 - f_2)/(f_1 + f_2)$ which is between 10^{-4} and 10^{-3} in our runs.

Carefully controlling this parameter is an interesting issue: recently, in a very similar von Kármán flow in the positive sense of rotation at high Re, de la Torre & Burguete (2007) reported bistability and a turbulent bifurcation at exactly $\epsilon = 0$ between two $\mathscr{R}_\pi$-symmetric flows. For non-zero ϵ, the mixing layer lies slightly above or below the equator and it randomly jumps between these two symmetric positions when ϵ is carefully set to zero.

With our very small experimental ϵ, we satisfy theoretical predictions (Chossat 1993; Porter & Knobloch 2005) for the 1:2 spatial resonance or $k - 2k$ interaction mechanism with slightly broken reflection symmetry. Instead of mixed mode, pure mode and heteroclinic cycles – specific to $O(2)$ and carefully reported by Nore *et al.* (2003, 2004, 2005) – we only observe drifting instability patterns, i.e. travelling waves and modulated travelling waves, characteristic of $SO(2)$. Also, the drift frequency is very close to zero at the threshold $Re_c = 330$ (figure 6*a*), in agreement with the prediction $f_D \sim O(\epsilon)$ (Chossat 1993; Porter & Knobloch 2005). This bifurcation to travelling waves is similar to the one-dimensional drift instability of steady patterns, observed in many systems (see e.g. Fauve *et al.* 1991). It relies on the breaking of the parity ($\theta \to -\theta$) of the pattern (Coullet & Iooss 1990): the travelling-wave pattern is a pair of tilted vortices. The bifurcation is an imperfect pitchfork (Porter & Knobloch 2005).

Finally, the comparison can be extended to the travelling waves observed with flat disks above the mixed and pure modes (Nore *et al.* 2003, 2005). The observed wave frequencies are of the same order of magnitude in both cases, which led us to believe that the same kind of hydrodynamics is involved , i.e. the blades again play a minor role at these low Reynolds numbers. However, the frequency ratio between the basic waves (TW) and their modulations (MTW) at onset is much higher ($\sim$32) in our experiment than in the numerical simulations ($\sim$5) (Nore *et al.* 2003). This could be due to the large number of blades.

We also consider the symmetry of the von Kármán flow with respect to the rotation axis. In fact, the time-averaged flow is exactly axisymmetric while the instantaneous flow is not, because of the presence of blades. However, axisymmetry can be considered as an effective property at low Reynolds number and at least up to $Re = 175$, since we have shown that the blades have almost no effect on the flow (see § 5.1). With increasing Re, the blades start playing their role and effectively break the axisymmetry of the instantaneous flow.

Finally, we emphasize that the observations made below $Re \sim 400$ closely resemble the route to chaos through successive symmetry breaking for low-degree-of-freedom dynamical systems. Our system can thus be considered as a small system (consistent with the aspect ratio which is of order of 1) until the Reynolds number becomes high enough to excite small dynamical scales in the flow.

6.2. *The three scales of the von Kármán flow*

The observations reported in this article from visualizations and spectra showed three different scales. In particular, time-spectra contain two time–frequency domains,

above and below the injection frequency $f_a = f$. Let us first roughly sketch the correspondence between temporal and spatial frequency scales of the whole flow:

(i) the smallest spatial frequencies, at the scale of the vessel, describe the basic swirling flow due to the impeller and produce the intermediate frequency range, i.e. the peak at $f_a = f$ in the time spectrum;

(ii) the intermediate spatial frequencies due to the shear-layer main instabilities produce the lowest time frequencies;

(iii) the highest spatial frequencies produce, of course, the highest temporal frequencies, i.e. the Kolmogorov region.

Taylor's hypothesis is based on a linear mapping between space and time frequencies. It is probably valid for the high part of the spectrum, but the mapping might not be linear and even not monotonic for the low part. We discuss each part of the spectrum in the two following sections.

6.2.1. *The $1/f$ low-frequency spectrum*

Once chaos is reached at $Re = 400$, a strong continuous and monotonic low-frequency spectrum is generated (figure 3*h*). In the chaotic regime below $Re \sim 1000$, the spectrum evolves to a neat -1 power law. Then, this part of the spectrum does not evolve any more with Re.

Low-frequency -1 exponents in spectra are common and could be due to a variety of physical phenomena: so-called '$1/f$ noises' have been widely studied, e.g. in the condensed matter field (see for instance Dutta & Horn 1981).

For turbulent von Kármán flows driven by two counter-rotating impellers, this low-time-scale dynamics has been already observed in liquid helium over at least a decade by Zocchi *et al.* (1994) as well as for the magnetic induction spectrum in liquid metals (Bourgoin *et al.* 2002; Volk, Odier & Pinton 2006). However, experiments carried out in a one-cell flow – without turbulent a mixing layer – did not show this behaviour (Marié 2003; Ravelet *et al.* 2004; Ravelet 2005). We therefore conclude that the $1/f_a$-spectrum is related to the chaotic wandering of the mixing layer which statistically restores the axisymmetry. Once again, the mixing layer slow dynamics dominates the whole dynamics of our system, from momentum transfer (Marié & Daviaud 2004) to the very high level of turbulent fluctuations (figures 5 and 8).

Furthermore, we can make the hypothesis that the -1 slope is due to the distribution of persistence times on each side of the bimodal distribution (figure 8): the low-frequency part of the spectrum can be reproduced by a random binary signal. Similar ideas for the low-frequency spectral construction are proposed for the magnetic induction in the von Kármán sodium (VKS) experiment (Ravelet *et al.* 2007). In both cases, longer statistics would be needed to confirm this idea.

6.2.2. *The turbulent fluctuations*

We show above how the flow transitions from chaos to turbulence between $Re \simeq 1000$ and $Re_t = 3300$. We label this region 'transition to turbulence' and observe the growth of a power-law region in the time-spectra for $f_a > f$. Does this slope trace back the Kolmogorov cascade in the space-spectra?

As the classical Taylor hypothesis cannot apply to our full range spectrum, we follow the local Taylor hypothesis idea (Pinton & Labbé 1994) for the high-frequency part $f_a > f$. Whereas Pinton & Labbé (1994) did not apply their technique (using instantaneous velocity instead of a constant advection) to the extreme case of zero advection, we think it can be applied here owing to the shape of the azimuthal velocity PDF (figure 8). These distributions show first that the instantaneous zero

velocity is a quite rare event: a local minimum of the curve. The modulus of velocity spends typically 75 % of the time between $\frac{1}{2}V_m$ and $\frac{3}{2}V_m$, where $\pm V_m$ are the positions of the PDF maxima. The sign of the advection has no effect on the reconstructed wavenumber. We can thus conclude that the frequency and wavenumber moduli can be matched to each other at first order by a factor equal to the most probable velocity $|V_m|$ or by the mean of $|v_\theta|$, very close to each other. This approach is consistent with a binary view of the local turbulent signal jumping randomly between two opposite mean values, just as in the turbulent flow reversal model of, e.g. Benzi (2005). Then, the high-frequency part of the spectrum is equivalent to the spectrum obtained by averaging the spectra of every time-series between jumps, while the low-frequency part is dominated by dynamics of the jumps themselves.

Owing to these arguments, we are convinced that an algebraic region dominates the high-frequency part of the k-spectra above Re_t. Observed exponents (-1.55) are of the order of the Kolmogorov exponent, less than 10 % smaller in absolute value. Similar exponents are also encountered at other locations in the vessel.

6.3. *Conclusion and perspectives*

The von Kármán shear flow with inertial stirring has been used for a global study of the transition from order to turbulence. The transition scenario is consistent with a globally supercritical scenario and this system appears to be a very powerful table-top prototype for such a type of study. We have chosen to consider a global view over a wide range of Reynolds number. This allowed us to make connections between information from local (velocities) or global quantities (torques, flow symmetries), as discussed in §§ 5.2, 6.1 and 6.2.

6.3.1. *Further work*

It would be interesting to increase the resolution of the analysis to the different observed thresholds. It would also be worth performing the same wide-range study for the other sense of rotation (+) or another pair of impellers. These studies would enable a comparison of the inertial effects on the turbulent dynamics at very high Reynolds number.

6.3.2. *Controlling the mixing layer*

Many results of the present study proceed from velocity data collected in the middle of the shear layer and we have shown that this layer and its chaotic/turbulent wandering can be responsible for the low-frequency content of the chaotic/turbulent spectrum of the data.

With the slightly different point of view of controlling the disorder level, we have modified the dynamics of the shear layer by adding a thin annulus located in the mid-plane of the flow (Ravelet *et al.* 2005). This property was recently used in the von Kármán Sodium (VKS) experiment conducted at Cadarache, France and devoted to the experimental study of dynamo action in a turbulent liquid-sodium flow. A dynamo has effectively been observed for the first time in this system with a von Kármán configuration using, among other characteristics, an annulus in the mid-plane (Monchaux *et al.* 2007) and is sensitive to the presence of this device. Moreover, clear evidence has been found that the mixing-layer large-scale patterns have a strong effect on the magnetic field induction at low frequency (Volk *et al.* 2006; Ravelet *et al.* 2007). Further studies of this effect in water experiments are in progress.

6.3.3. *Statistical properties of the turbulence*

Studies of the von Kármán flow currently in progress involve both a wider range of data in space, with the use of stereoscopic 3-components particle image velocimetry (SPIV) and a wider range of Reynolds number.

Whereas the SPIV is slower than LDV and will not allow time-spectral analysis, it offers a global view of the flow and allows characterization of statistical properties of the turbulent velocity. Guided by the behaviour of the variance of the local azimuthal velocity revealed in the present article (figure 5), we expect to analyse the evolution of the spatio-temporal statistical properties with *Re*. Such a study is very stimulating for theoretical advances in statistical mechanics of turbulence in two-dimensional (Robert & Sommeria 1991; Chavanis & Sommeria 1998), quasi-two-dimensional (Bouchet & Sommeria 2002; Jung, Morrison & Swinney 2006) or axisymmetric flows (Leprovost, Dubrulle & Chavanis 2006; Monchaux *et al.* 2006).

We are particularly indebted to Vincent Padilla and Cécile Gasquet for building and piloting the experiment. We acknowledge Caroline Nore for making her simulations available, Arnaud Guet for his help with the visualizations and Frédéric Da Cruz for the viscosity measurements. We have benefited from very fruitful discussions with B. Dubrulle, N. Leprovost, L. Marié, R. Monchaux, C. Nore, J.-F. Pinton and R. Volk.

REFERENCES

Batchelor, G. K. 1951 Note on a class of solutions of the Navier-Stokes equations representing steady rotationally-symmetric flow. *Q. J. Mech. App. Maths* **4**, 29.

Benzi, R. 2005 Flow reversal in a simple dynamical model of turbulence. *Phys. Rev. Lett.* **95**, 024502.

Bouchet, F. & Sommeria, J. 2002 Emergence of intense jets and Jupiter's great red spot as maximum-entropy structures. *J. Fluid Mech.* **464**, 165.

Bourgoin, M., Marié, L., Pétrélis, F., Gasquet, C., Guigon, A., Luciani, J.-B., Moulin, M., Namer, F., Burguete, J., Chiffaudel, A., Daviaud, F., Fauve, S., Odier, P. & Pinton, J.-F. 2002 MHD measurements in the von Kármán sodium experiment. *Phys. Fluids* **14**, 3046.

Buchhave, P., George, W. K. & Lumley, J. L. 1979 The measurement of turbulence with the Laser-Doppler anemometer. *Annu. Rev. Fluid Mech.* **11**, 443.

Cadot, O., Couder, Y., Daerr, A., Douady, S. & Tsinober, A. 1997 Energy injection in closed turbulent flows: Stirring through boundary layers versus inertial stirring. *Phys. Rev.* E **56**, 427.

Cadot, O., Douady, S. & Couder, Y. 1995 Characterization of the low-pressure filaments in a three-dimensional turbulent shear flow. *Phys. Fluids* **7**, 630.

Chavanis, P.-H. & Sommeria, J. 1998 Classification of robust isolated vortices in two-dimensional hydrodynamics. *J. Fluid Mech.* **356**, 259.

Chossat, P. 1993 Forced reflexional symmetry breaking of an *o(2)*-symmetric homoclinic cycle. *Nonlinearity* **6**, 723.

Coullet, P. & Iooss, G. 1990 Instabilities of one-dimensional cellular patterns. *Phys. Rev. Lett.* **64**, 866.

Douady, S., Couder, Y. & Brachet, M. E. 1991 Direct observation of the intermittency of intense vorticity filaments in turbulence. *Phys. Rev. Lett.* **67**, 983.

Dutta, P. & Horn, P. M. 1981 Low-frequency fluctuations in solid: 1/f noise. *Rev. Mod. Phys.* **53**, 497.

Escudier, M. P. 1984 Observations of the flow produced in a cylindrical container by a rotating endwall. *Exps. Fluids* **2**, 189.

Falkovich, G. 1994 Bottleneck phenomenon in developed turbulence. *Phys. Fluids* **6**, 1411.

Fauve, S., Douady, S. & Thual, O. 1991 Drift instabilities of cellular patterns. *J. Phys.* II **1**, 311.

Fauve, S., Laroche, C. & Castaing, B. 1993 Pressure fluctuations in swirling turbulent flows. *J. Phys.* II **3**, 271.

Frisch, U. 1995 *Turbulence – The Legacy of A. N. Kolmogorov*. Cambridge University Press.

Gauthier, G., Gondret, P. & Rabaud, M. 1999 Axisymmetric propagating vortices in the flow between a stationary and a rotating disk enclosed by a cylinder. *J. Fluid Mech.* **386**, 105.

Gelfgat, A. Y., Bar-Yoseph, P. Z. & Solan, A. 1996 Steady states and oscillatory instability of swirling flow in a cylinder with rotating top and bottom. *Phys. Fluids* **8**, 2614.

Gioia, G. & Chakraborty, P. 2006 Turbulent friction in rough pipes and the energy spectrum of the phenomenological theory. *Phys. Rev. Lett.* **96**, 044502.

Goldenfeld, N. 2006 Roughness-induced critical phenomena in a turbulent flow. *Phys. Rev. Lett.* **96**, 044503.

Harriott, G. M. & Brown, R. A. 1984 Flow in a differentially rotated cylindrical drop at moderate Reynolds number. *J. Fluid Mech.* **144**, 403.

Hodgman, C. D. (Ed.) 1947 *Handbook of Chemistry and Physics,* 30th Edn. Chemical Rubber Publishing Co.

Jung, S. W., Morrison, P. J. & Swinney, H. L. 2006 Statistical mechanics of two-dimensional turbulence. *J. Fluid Mech.* **554**, 433.

von Kármán, T. 1921 Über laminäre und turbulente Reibung. *Z. Angew. Math. Mech.* **1**, 233.

Knobloch, E. 1996 Symmetry and instability in rotating hydrodynamic and magnetohydrodynamic flows. *Phys. Fluids* **8**, 1446.

Labbé, R., Pinton, J.-F. & Fauve, S. 1996 Power fluctuations in turbulent swirling flows. *J. Phys* II **6**, 1099.

La Porta, A., Voth, G. A., Crawford, A. M., Alexander, J. & Bodenschatz, E. 2001 Fluid particle acceleration in fully developed turbulence. *Nature* **409**, 1017.

Lathrop, D. P., Fineberg, J. & Swinney, H. L. 1992 Transition to shear-driven turbulence in Couette-Taylor flow. *Phys. Rev.* A **46**, 6390.

Leprovost, N., Dubrulle, B. & Chavanis, P.-H. 2006 Dynamics and thermodynamics of axisymmetric flows: Theory. *Phys. Rev.* E **73**, 046308.

Leprovost, N., Marié, L. & Dubrulle, B. 2004 A stochastic model of torque in von Kármán swirling flow. *Euro. Phys. J.* B **39**, 121.

Lesieur, M. 1990 *Turbulence in Fluids*, 2nd Revised Edn. Kluwer.

Lohse, D. & Müller-Groeling, A. 1995 Bottleneck effects in turbulence: Scaling phenomena in r versus p space. *Phys. Rev. Lett.* **74**, 1747.

Manneville, P. 1990 *Dissipative Structures and Weak Turbulence*. Academic.

Marié, L. 2003 Transport de moment cinétique et de champ magnétique par un écoulement tourbillonaire turbulent: influence de la rotation. PhD thesis, Université Paris VII.

Marié, L., Burguete, J., Daviaud, F. & Léorat, J. 2003 Numerical study of homogeneous dynamo based on experimental von Kármán type flows. *Euro. Phys. J.* B **33**, 469.

Marié, L. & Daviaud, F. 2004 Experimental measurement of the scale-by-scale momentum transport budget in a turbulent shear flow. *Phys. Fluids* **16**, 457.

Mellor, G. L., Chapple, P. J. & Stokes, V. K. 1968 On the flow between a rotating and a stationary disk. *J. Fluid Mech.* **31**, 95.

Moisy, F., Willaime, H., Andersen, J. S. & Tabeling, P. 2001 Passive scalar intermittency in low temperature helium flows. *Phys. Rev. Lett.* **86**, 4827.

Monchaux, R., Berhanu, M., Bourgoin, M., Moulin, M., Odier, Ph., Pinton, J.-F., Volk, R., Fauve, S., Mordant, N., Pétrélis, F., Chiffaudel, A., Daviaud, F., Dubrulle, B., Gasquet, C., Marié, L. & Ravelet, F. 2007 Generation of magnetic field by dynamo action in a turbulent flow of liquid sodium. *Phys. Rev. Lett.* **98**, 044502.

Monchaux, R., Ravelet, F., Dubrulle, B., Chiffaudel, A. & Daviaud, F. 2006 Properties of steady states in turbulent axisymmetric flows. *Phys. Rev. Lett.* **96**, 124502.

Nikuradse, J. 1932 Gesetzmassigkeiten der turbulenten Stromungen in glatten Rohren. *vDI Forshungsheft* 356, (English transl. NASA TT F-10 (1966), p. 359).

Nikuradse, J. 1933 Stromungsgesetz in rauhren Rohren. *vDI Forshungsheft* 361, (English transl. *Tech. Mem.* 1292, NACA (1950)).

Nore, C., Moisy, F. & Quartier, L. 2005 Experimental observation of near-heteroclinic cycles in the von Kármán swirling flow. *Phys. Fluids* **17**, 064103.

Nore, C., Tartar, M., Daube, O. & Tuckerman, L. S. 2004 Survey of instability thresholds of flow between exactly counter-rotating disks. *J. Fluid Mech.* **511**, 45.

Nore, C., Tuckerman, L. S., Daube, O. & Xin, S. 2003 The 1:2 mode interaction in exactly counter-rotating von Kármán swirling flow. *J. Fluid Mech.* **477**, 51.

Ouellette, N. T., Xu, H., Bourgoin, M. & Bodenschatz, E. 2006 Small-scale anisotropy in Lagrangian turbulence. *New J. Phys.* **8**, 102.

Pinton, J.-F. & Labbé, R. 1994 Correction to the Taylor hypothesis in swirling flows. *J. Phys.* II **4**, 1461.

Porter, J. & Knobloch, E. 2005 Dynamics in the 1:2 spatial resonance with broken reflection symmetry. *Physica* D **201**, 318–344.

Ravelet, F. 2005 Bifurcations globales hydrodynamiques et magnétohydrodynamiques dans un écoulement de von Kármán turbulent. PhD thesis, Ecole Polytechnique, France.

Ravelet, F., Chiffaudel, A., Daviaud, F. & Leorat, J. 2005 Toward an experimental von Kármán dynamo: Numerical studies for an optimized design. *Phys. Fluids* **17**, 117104.

Ravelet, F., Marié, L., Chiffaudel, A. & Daviaud, F. 2004 Multistability and memory effect in a highly turbulent flow: Experimental evidence for a global bifurcation. *Phys. Rev. Lett.* **93**, 164501.

Ravelet, F., Volk, R., Behranu, M., Chiffaudel, A., Daviaud, F., Dubrulle, B., Fauve, S., Monchaux, R., Mordant, N., Odier, Ph., Pétrélis, F. & Pinton, J.-F. 2007 Magnetic induction in a turbulent flow of liquid sodium: mean behaviour and slow fluctuations. Phys. Fluids (submitted).

Robert, R. & Sommeria, J. 1991 Statistical equililbrium states for two-dimensional flows. *J. Fluid Mech.* **229**, 291.

Schlichting, H. 1979 *Boundary-Layer Theory*, 7th Edn. McGraw-Hill.

Schouveiler, L., Le Gal, P. & Chauve, M.-P. 2001 Instabilities of the flow between a rotating and a stationary disk. *J. Fluid Mech.* **443**, 329.

Sørensen, J. B. & Christensen, E. A. 1995 Direct numerical simulation of rotating fluid flow in a closed cylinder. *Phys. Fluids* **7**, 764.

Spohn, A., Mory, M. & Hopfinger, E. J 1998 Experiments on vortex breakdown in a confined flow generated by a rotating disc. *J. Fluid Mech.* **370**, 73.

Stewartson, K. 1953 On the flow between two rotating coaxial disks. *Proc. Camb. Phil. Soc.* **49**, 333.

Tabeling, P., Zocchi, G., Belin, F., Maurer, J. & Willaime, H. 1996 Probability density functions, skewness and flatness in large Reynolds number turbulence. *Phys. Rev.* E **53**, 1613.

Tennekes, H. & Lumley, J. L. 1972 *A First Course in Turbulence*. MIT Press.

Titon, J.-H. & Cadot, O. 2003 The statistics of power injected in a closed turbulent flow: Constant torque forcing versus constant velocity forcing. *Phys. Fluids* **15**, 625.

de la Torre, A. & Burguete, J. 2007 Slow dynamics in a turbulent von Kármán swirling flow. *Phys. Rev. Lett.* **99**, 054101.

Volk, R., Odier, P. & Pinton, J.-F. 2006 Fluctuation of magnetic induction in von Kármán swirling flows. *Phys. Fluids* **18**, 085105.

Zandbergen, P. J. & Dijkstra, D. 1987 von Kármán swirling flows. *Annu. Rev. Fluid Mech.* **19**, 465.

Zocchi, G., Tabeling, P., Maurer, J. & Willaime, H. 1994 Measurement of the scaling of the dissipation at high Reynolds numbers. *Phys. Rev.* E **50**, 3693.